Science Advances

AAAS

advances.sciencemag.org/cgi/content/full/3/6/e1700512/DC1

Supplementary Materials for

Nonvolatile ferroelectric domain wall memory

Pankaj Sharma, Qi Zhang, Daniel Sando, Chi Hou Lei, Yunya Liu, Jiangyu Li,
Valanoor Nagarajan, Jan Seidel

Published 23 June 2017, *Sci. Adv.* **3**, e1700512 (2017)
DOI: 10.1126/sciadv.1700512

This PDF file includes:

- Supplementary Text
- fig. S1. X-ray characterization of a BFO/STO (110) film.
- fig. S2. E-beam lithography and metal deposition procedure.
- fig. S3. DW device.
- fig. S4. BFO/STO (110) coplanar switching kinetics.
- fig. S5. Vector PFM of the switched domain.
- fig. S6. A schematic of the ferroelectric switching process (top view).
- fig. S7. Electrical poling of the BFO/LSMO/STO (110).
- fig. S8. Numerical simulation of the switched ferroelastic domain.
- fig. S9. Triangular or the arrow-like shape of the switched domain.
- fig. S10. Switching via electric field oriented 45° to the in-plane polarization direction.
- fig. S11. Sub–100-nm FEDW memory device.
- fig. S12. Potential and electric field distribution.
- fig. S13. Integration of FEDW memory cell in an array structure.
- References (*36*–*38*)

Supplementary Text

I. Structural characterization of the $BiFeO_3$ thin film

To ascertain the structural properties of our BFO films, we used x-ray diffraction (XRD) and x-ray reflectometry (XRR). In fig. S1, we describe the exact sample with which all the results of this manuscript were obtained. First, we use a standard coupled θ/2θ scan to confirm that the film is in a single phase: the pattern in fig. S1A exhibits only (HH0) peaks from the film and substrate (as indexed), with no evidence of parasitic phases.

In order to understand the ferroelastic domain configuration, we used XRD reciprocal space mapping (RSMs). It is well-documented that when grown epitaxially on (110)-oriented STO substrates, BFO typically forms in a monoclinic M_B structure (*36, 37*). To confirm this for our film and to understand its twinning structure, we used RSMs with two different values of the azimuthal angle φ (figs. S1, B and C). The first set of scans (with φ = 0) allows us access to the symmetric (220), and asymmetric (221) reflections. The RSM around (220) (φ = 0) yields a single, rather narrow BFO peak, consistent with a single phase with a narrow distribution of tilting of the lattice planes (in the out-of-plane direction) parallel to the [001] direction. For the (221) reflection, on the other hand, the BFO peak, while aligned vertically with the substrate (reflecting the strained nature of the film) shows a clear splitting, which is the hallmark of a monoclinic distortion (where each peak corresponds to a particular monoclinic domain). We note here that the average out-of-plane position of the two peaks aligns perfectly with the out-of-plane position of the (220) BFO peak in fig. S1B, confirming that the splitting is indeed due to a monoclinic structure. Upon rotation of the sample by φ = 90° (figs. S1, D and E), we gain access once again to the symmetric (220) reflection, but also to the (210) asymmetric reflection, which together provide complementary information about the out-of-plane mosaicity and the distribution of in-plane lattice parameters, respectively. As for the φ = 0 case, the (220) reflection (φ = 90) yields a single BFO peak, albeit with a much broader shape, implying that there is a much larger distribution of tilting of the (HH0) lattice planes along the [1-10] direction. For the (210) reflection (φ = 90) we see a single BFO peak which is not aligned vertically with the substrate peak, revealing that i) no twinning occurs and ii) the film is not strained, along this direction. The rather broad nature of this peak implies that a larger distribution of in-plane-lattice constant is present for the BFO film along the [1-10] direction. The twinning structure and difference in peak widths along the orthogonal [001] and [1-10] directions is consistent with two possible mechanisms for relaxation of mismatch strain: by twinning domains (as we see here in the [001] direction), or by lattice relaxation (as we see here in the [1-10] direction). From the RSMs and the θ/2θ scans we derive the following lattice parameters for our film (the monoclinic M_B structure (with unit vectors) and its relation to the STO (110) substrate is shown in fig. S1F

a_{mc} = 5.677 Å (// $[110]_{pc}$)

b_{mc} = 5.619 Å (// $[-110]_{pc}$)

c_{mc} = 3.905 Å (// $[001]_{pc}$)

β_{mc} = 89.2°

In summary, this RSM analysis indicates that we have a BFO film that is well crystallized (and completely strained) in the [001] direction, while along the [1-10] direction the film is relaxed and shows poorer crystallinity.

To determine the film thickness, we used X-ray reflectometry (XRR). The XRR spectrum in fig. S1G shows a reasonable number of oscillations, consistent with a surface that has some roughness as observed in AFM scans. The thickness of this film, extracted from fitting of the spectrum, is 53 nm. In addition, we find an interface roughness value of 0.15 nm, and a surface roughness value of 1.2 nm; the latter being consistent with measurements by AFM. Finally, to ensure that the epitaxial relationship between substrate and film is indeed cube-on-cube, φ scans at the (111) Bragg condition for the substrate and film, were performed. As shown in fig. S1H, both the substrate and film reflections exhibit two-fold rotational symmetry in φ, confirming cube-on-cube epitaxy.

II. Electron-beam patterning of the devices

After establishing structural characteristics of the BFO thin film, the devices were fabricated on the surface of the film. Figure S2 presents a pictorial visualization of the entire device patterning procedure via e-beam nanolithography and physical vapor deposition (PVD) techniques. A positive resist of Polymethyl methacrylate (PMMA) was first deposited on a BFO/STO thin film by spin coating to form an approximately 150-200 nm thick resist layer (figs. S2, A and B). After prebaking, the film was put into a FEI Sirion Scanning Electron Microscope chamber for lithography. In this process, a designed pattern was scanned by electron-beam (fig. S2C), which causes a change in the solubility of the exposed PMMA and is removed in the following developing process (fig. S2D), while unexposed PMMA areas remain intact on the film even after developing. After that, Ti and Pt coatings were deposited on the film, successively. Firstly, a 3 nm thick Ti layer was deposited to enhance the adhesion of the subsequent Pt layer (12 nm) on the BFO film (fig. S2E). Then, the film with the Pt/Ti coatings was put in the N-Methyl-2-pyrrolidone (NMP) solvent, which dissolves the PMMA at 80 °C. This step removes Pt/Ti coatings outside the developed areas i.e., in regions where there is an underneath layer of PMMA. After removal of metal outside the developed areas, the desired prototype device pattern is realized and is used for the further SPM measurements (fig. S2F).

The topographic maps in fig. S3 display representative images of the actual fabricated device. From topographic images, the (nearly) circular Pt electrode of radius approx. 200 nm is much smaller in size compared to the counter large rectangular Pt electrode (of dimensions approx. 10 μm x 20 μm; thickness of both the electrodes is approx. 15 nm). The spacing between the metal electrodes is about 300 nm.

III. As-grown state and details of the ferroelectric switching

Figure S4 shows lateral (LPFM) and vertical PFM (VPFM) images for the as-grown state as well after application of an external switching field (corresponding to Figs. 1,D to E in the main text). As can be seen, vertical PFM amplitude (VPFM-a) and phase (VPFM-p) images remain unchanged, while lateral PFM images reveal 71° ferroelastic switching. Further LPFM imaging (fig. S5) of the switched domain along two orthogonal in-plane crystallographic directions confirms the absence of polarization along the [1-10]/[-110] direction. For LPFM in [1-10]/[-110] direction (figs. S5, C and D), no domain or domain walls are seen and the observed lateral PFM amplitude is extremely low in agreement with the absence of polarization. Also, the application of switching in-plane electric field along the [1-10]/[-110] direction (via nano-patterning metal electrodes perpendicular to the morphological stripes) did not affect polarization due to the lateral component of the polarization pointing along [001]/[00-1] direction.

Figure S6 shows a schematic of the ferroelectric switching process (top view). Polarization reversal or switching of domains in ferroelectric materials comprises of two basic features, i.e. the creation of a reverse polarized domain together with the spontaneous appearance of ferroelectric domain walls. Polarization reversal in ferroelectric systems is described by a three-stage process (*31*). The stages of switching are as follows (fig. S6): firstly, formation of a reverse polarized nucleus and the spontaneous appearance of FEDWs; secondly, rapid forward growth of the reversed polarized nucleus towards the counter metal electrode; and finally, slower sideways domain expansion of the switched domain. During this entire switching sequence, FEDWs reconfigure simultaneously with the shape of the switched ferroelectric domain. In Fig. 1(E), the PFM image shows the non-volatile configuration of the switched domain and FEDWs after removal of the switching electric-field.

To determine orientation of the out-of-plane polarization component (fig. S7), PFM measurements were performed on a blanket BFO thin film (approx. 80 nm) grown on STO (110) substrate with a conductive buffer layer of $LaSr_xMn_{1-x}O_3$ (LSMO) as the bottom electrode. A bipolar domain state was created via electrical poling of the concentric square regions (inner region: +7V, outer region: -7V) using a biased conductive SPM tip. The electrical poling results confirm that the out-of-plane component of the ferroelectric polarization is oriented (downwards) towards the bottom interface for the (110) BFO thin films.

IV. Phase-field simulations of the switched ferroelastic domain

Numerical simulation is implemented to capture the domain pattern and its evolution corresponding to the experimental study. The potential distribution induced by the two platinum metal electrodes on top of BFO and STO is first simulated by finite element method using COMSOL Electrostatic Module (fig. S8A). The corresponding electric field is then passed to a phase field simulation as an external electrical input to the model system. It uses characteristic functions of ferro-electric variants to represent configurations and evolutions of domains patterns, which is subjected to the constraints of mechanical and electric equilibrium. The deviation from the equilibrium state provides the driving force for the domain formation, and the evolution equations are solved by semi-implicit finite difference method on the temporal scale and fast Fourier transform on the spatial scale.

To be specific, two participating polarization variants, denoted by P_1^- and P_2^-, are considered in the phase field simulation (*38*). The topology of the variants is described by one characteristic function ($\mu(\mathbf{x})$) to indicate the existences as follows

$$\mu(\mathrm{x}) = \begin{cases} 0 & \mathrm{x} \in P_1^- \\ 1 & \mathrm{x} \in P_2^- \end{cases} \tag{S1}$$

The distribution of the variants in the material system induces inhomogeneous eigen-strains (ε^s) and spontaneous polarizations (P^s) denoted by

$$\begin{aligned} \varepsilon^s(\mathrm{x}) &= (1-\mu(\mathrm{x}))\varepsilon_1^- + \mu(\mathrm{x})\varepsilon_2^- \\ P^s(\mathrm{x}) &= (1-\mu(\mathrm{x}))P_1^- + \mu(\mathrm{x})P_2^- \end{aligned} \tag{S2}$$

which are simply the linear combination of the eigen-strains and polarizations of the variants. The material system obeys the elastic equilibrium and the Maxwell equations subjected to external electric field induced by the platinum electrode pair.

The formation and evolution of microstructure is governed by the variation of the energy functional as the driving force

$$\frac{\partial \mu}{\partial t} = L\frac{\delta W}{\delta \mu} \tag{S3}$$

where L is the mobility constant and $W(\mu)$ is the total energy of the material system that consists of interfacial, anisotropic, elastic, and electric contributions, together with work done from external stress and external electric field. $W(\mu)$ can be written as

$$W(\mu) = \int_{\Omega}\left(A\left|\nabla \mu\right|^2 + k\mu^2(1-\mu)^2 + \frac{1}{2}(\varepsilon - \varepsilon^s(\mu))\cdot C(\varepsilon - \varepsilon^s(\mu)) - E^{ext}\cdot P - \sigma^{ext}\cdot \varepsilon \right) d\mathbf{x} + \frac{\varepsilon_0}{2}\int_{R^3}\left|\nabla \phi\right|^2 d\mathbf{x}$$

(S4)

The right-hand side of equation (S3) represents the total driving force of the system, which can be computed using variational derivatives (*38*). The phase field evolution equation (S3) can be explicitly expressed in the form of a diffusion equation with driving forces as the source term

$$\frac{\partial \mu}{\partial t} = D\nabla^2 \mu - \mu(1-\mu)(1-2\mu) + \frac{1}{2K}\sigma.\frac{\partial \varepsilon^s}{\partial \mu} + \frac{1}{2K}E.\frac{\partial P^s}{\partial \mu} \tag{S5}$$

where D is some normalized constant, and $E = E^{ext} - \nabla \phi$ is the effective electric field as the driving force. In the simulations, we used the following values for parameters: $D = 0.0001$ and $K = 10^9$. It is noted that the total electric field contribution includes the applied external electric field as well as the electric field induced by the instantaneous polarization of the evolving domain. In other words, the total electric field is the sum of the pre-calculated external electric field induced by the electric potential applied on the platinum electrode plates and the electric field induced by the domain structure evolution.

Under the effect of the applied electrical potential between the metal electrodes, the as-grown state comprising of polarization variant P_1^- switches to P_2^- (figs. S8, B and C). The polarization variant P_2^- nucleates and propagates in the direction of the applied field towards the counter large metal electrode. Thereafter, the domain expands sideways to attain an equilibrium configuration (figs. S8, C and D). The calculated equilibrium domain shows triangular-profile with rather diffuse edges and vertices. The simulation is qualitatively consistent with the experiment in the evidence that evolution of variants (P_1^-, and P_2^-) is activated and control by electric potential.

V. Arrow-head shaped domain of opposite in-plane polarity

The switched domains (DWs) are described as having triangular or arrow-like shape especially towards the end where they meet the counter large metal **(**Pt**)** electrode, because the switched domain (of different sizes) usually acquired an arrow-like shape or triangular protrusion with rather sharp facets (see figs. S9 and S10). However, in some cases the triangular protrusion was somewhat diffuse, but still can be seen in the overall shape.

Further, the intriguing observation of an arrow-head shaped domain of polarity opposite to the applied poling field direction was quite a common occurrence rather than an anomaly (fig. S9), and was resolved quite cleanly in our measurements (performed in non-resonant PFM mode). The same domain structure was also clearly reproduced (fig. S10), even when the orientation of the applied in-plane field was varied by 45° (by alternatively nano-patterning Pt electrodes at an angle of 45° with respect to the in-plane polarization direction). As before, the domain of opposite polarity (dark stripe in PFM phase) was clearly resolved in both the PFM amplitude and phase images (figs. S10, A and B). Moreover, no unusually high spurious changes in the PFM amplitude were observed at or near the domain of opposite polarity (dark stripe in PFM phase). Finally, the observed domain structure in our case was quite stable (figs. S10, C and D), which indicates its robustness and stability thermodynamically.

VI. Sub-100 nm domain wall memory device

Figure S11 shows operation of a prototype domain wall memory device with lateral length scale below 100 nm. In the presence of DWs of approx. 90 nm in length between the in-plane metal electrodes (figs. S11, A and B), the device is in the ON or the low resistance state. While, in the absence of DWs, the OFF state is achieved (figs. S11, C and D).

VII. Electric field and potential distribution between metal electrodes

To visualize distribution of the electric field and potential, finite element calculations were performed. The configuration of the finite element simulation consists of the material BFO subjected to electric effect generated by two platinum electrodes. The electric potential generated by the platinum electrode pair on the system is given by Maxwell's equation

$$\nabla \cdot (\varepsilon(\mathbf{x}) \nabla \phi(\mathbf{x})) = 0 \tag{S6}$$

where $\varepsilon(\mathbf{x})$ is the permittivity of the material and $\phi(\mathbf{x})$ is the electric potential.

The boundary conditions are the specified potentials on the region of the computational domain occupied by the platinum electrodes. To be specific, on the region on the top surface of the sample occupied by the large platinum electrode which is grounded, the potential is zero volt, while on the top surface of the sample occupied by the small platinum electrode where a voltage is applied, the potential is one volt. A mesh of the computational domain is automatically generated by the finite element software (COMSOL) into indexed four-noded tetrahedral elements and nodes. Each node is associated with coordinates $\mathbf{x}_i = (x_i, y_i, z_i)$ and nodal electric potentials $\phi_i\,(\mathbf{x}) = \phi(\mathbf{x}_i) = \phi(x_i, y_i, z_i)$. The electric potential at any point other than the nodes can be obtained through interpolation of elements that contains the requested point, via shape functions $N_j(x, y, z)$ associated with the involved element

$$\phi(x, y, z) = \sum_{j=1}^{\#nodes} N_j(x, y, z)\phi_j \tag{S7}$$

As a remark, the computation of shape functions are standard in finite element analysis, and can be given in the form

$$N_j(x,y,z) = a_j + b_j x + c_j y + d_j z \ ,$$

where the constants a_j, b_j, c_j, and d_j are determined from the coordinates of the nodes on the element.

The electric potentials at nodes are computed by solving the matrix equation

$$\mathbf{A}\phi = \mathbf{b} \tag{S8}$$

where $\mathbf{A}$ is the conductive matrix, ϕ is the vector storing the nodal potential, $\mathbf{b}$ is the vector relating boundary conditions.

The calculated electric potentials are visualized in a contour plot. The profile of electric potential is consistent with the applied potentials on the platinum electrode plates. The electric field is computed as the gradients of the potential

$$\mathbf{E}(\mathbf{x}) = -\nabla\phi(\mathbf{x}) \tag{S9}$$

This is computed and shown visually by COMSOL. The electric field is pointing in the direction of decreasing potential. This field then serves as the input to the phase field simulation as a part of the total electrical driving force. The distance (*d*) between the two platinum plate electrodes can be adjusted accordingly to study the resulting electric field distributions with different distance-thickness (*d*-*h*) ratios (*h* is the thickness of the ferroelectric film).

Figure S12 shows the calculated results obtained for two cases of different *d*-*h* ratios, i.e. for *d* = *2h*, and *d* = h. Note that the color contour shows the electrical potential, while the arrows in white represent vectors of the electric field. For the sake of clarity, electric fields (as arrows in white) are displayed in the region between the platinum electrode pair. These calculations reveal that the field is predominantly in-the-plane, and the out-of-plane component of the field is negligibly small (fig. S12). These calculated results agree with the obtained experimental coplanar switching results, which show that the out-of-plane component of the polarization remains unaffected (even for 90 nm domain wall devices).

VIII. Integration of FEDW memory cell in an array structure

The FEDW memory cell exhibits ON (Low R) and OFF (High R) state in the presence and absence of a FEDW interconnect, respectively. In our study, we have demonstrated a simple two-terminal device, which can easily be integrated in an array structure as shown in fig. S13A. Moreover, the specific in-plane geometry of FEDW memory cells can be varied. It was used in this study to unambiguously establish the central role of conductive FEDWs. The same concept can be implemented in vertical structures (out-of-plane capacitor geometry), where the nanostructured ferroelectric material is sandwiched between the metallic electrodes. The vertical geometry will allow integration of FEDW memory cells using already well established architectures such as cross-bar array structures (fig. S13B). Such that each cell in the 2D memory array can be identified by its unique Cartesian coordinates.

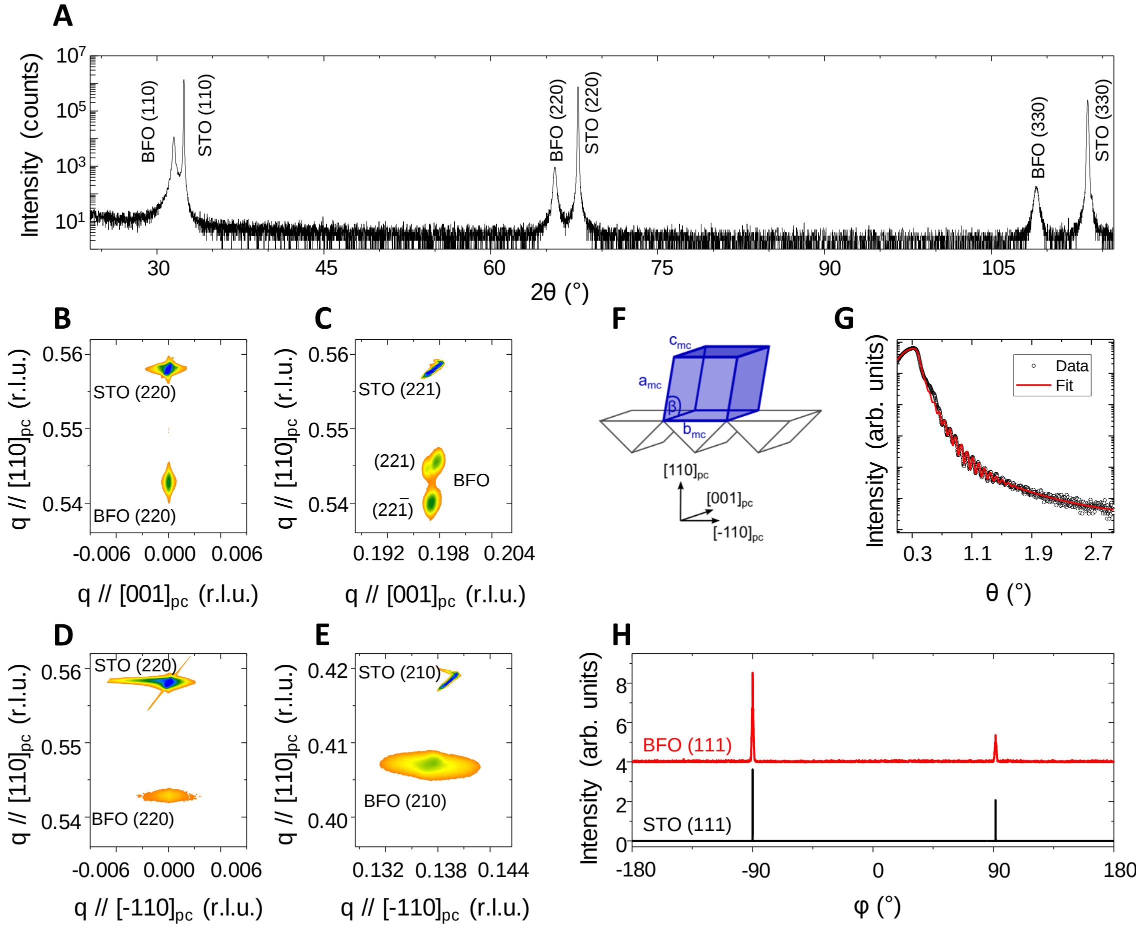

fig. S1. X-ray characterization of a BFO/STO (110) film. (**A**) θ-2θ X-ray diffraction scan. (**B** to **C**) Reciprocal scape maps along symmetric (220) (B), and antisymmetric (221) reflections (C), performed at azimuthal angle φ = 0°. (**D** to **E**) Reciprocal scape maps along symmetric (220) (D), and antisymmetric (210) reflections (E) performed at azimuthal angle φ = 90°. (**F**) A schematic of the monoclinic M_B structure of the film (with unit vectors) and its relation to the STO (110) substrate. (**G**) X-ray reflectometry measurement. (**H**) φ scans at the (111) Bragg condition for the substrate and film.

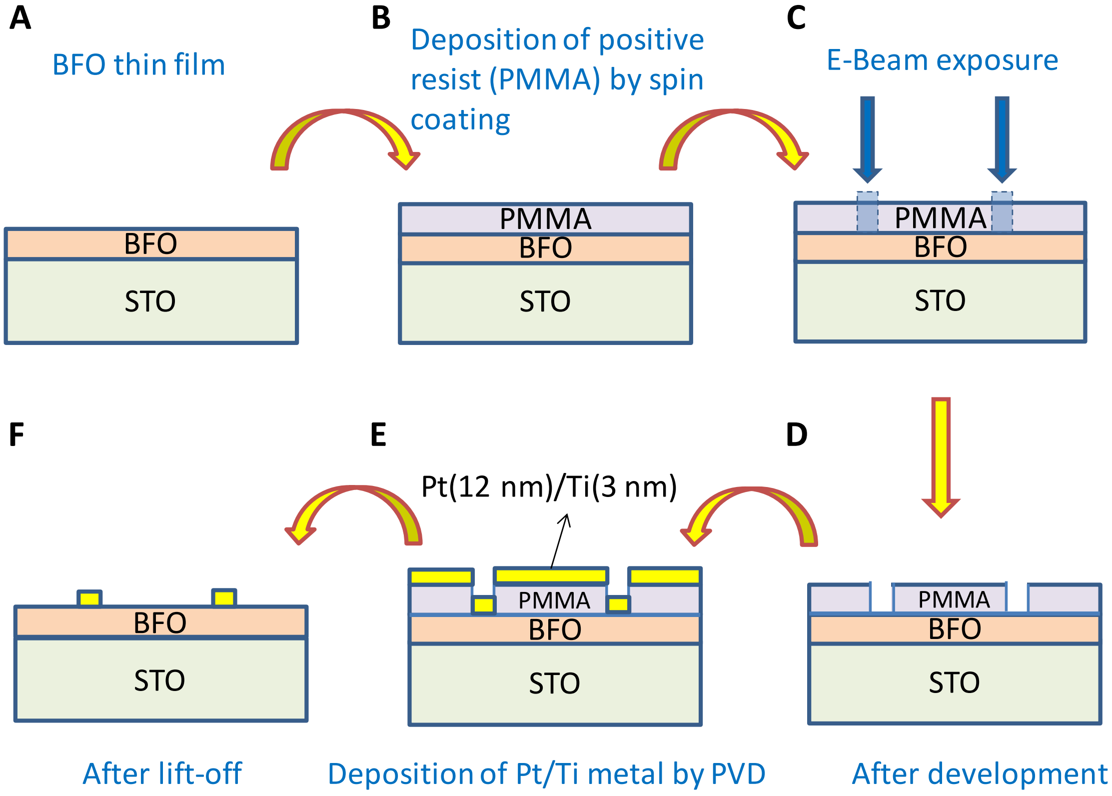

fig. S2. E-beam lithography and metal deposition procedure. A Schematic illustration of electron-beam lithography and metal deposition procedure.

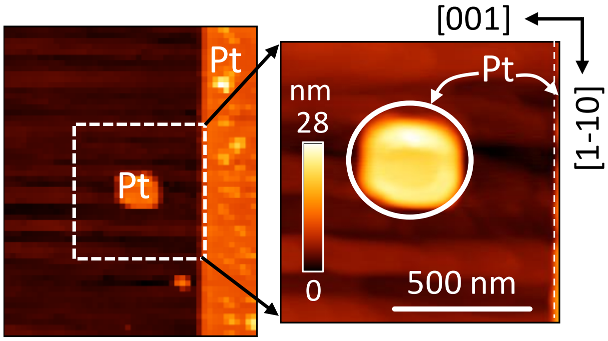

fig. S3. DW device. Topographic images of the electron-beam patterned domain wall device.

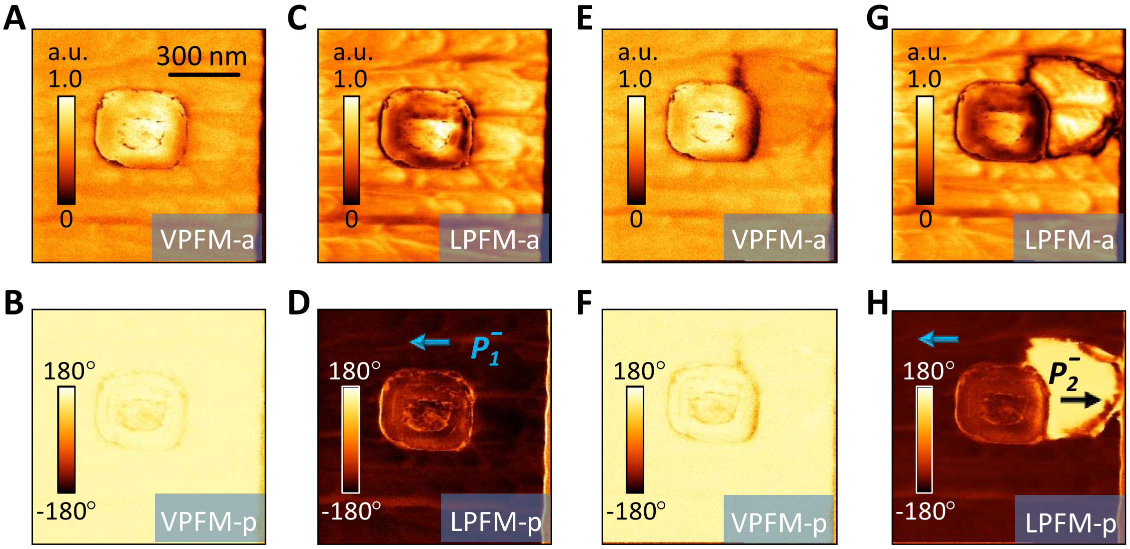

fig. S4. BFO/STO (110) coplanar switching kinetics. (**A** to **H**) PFM images for the as-grown state (A-D), and after application of an external switching field (E-H) respectively. Images in (A, E) represent vertical PFM amplitude and in (B, F) the corresponding vertical PFM phase. Images in (C, G) represent lateral PFM amplitude and in (D, H) the corresponding lateral PFM phase.

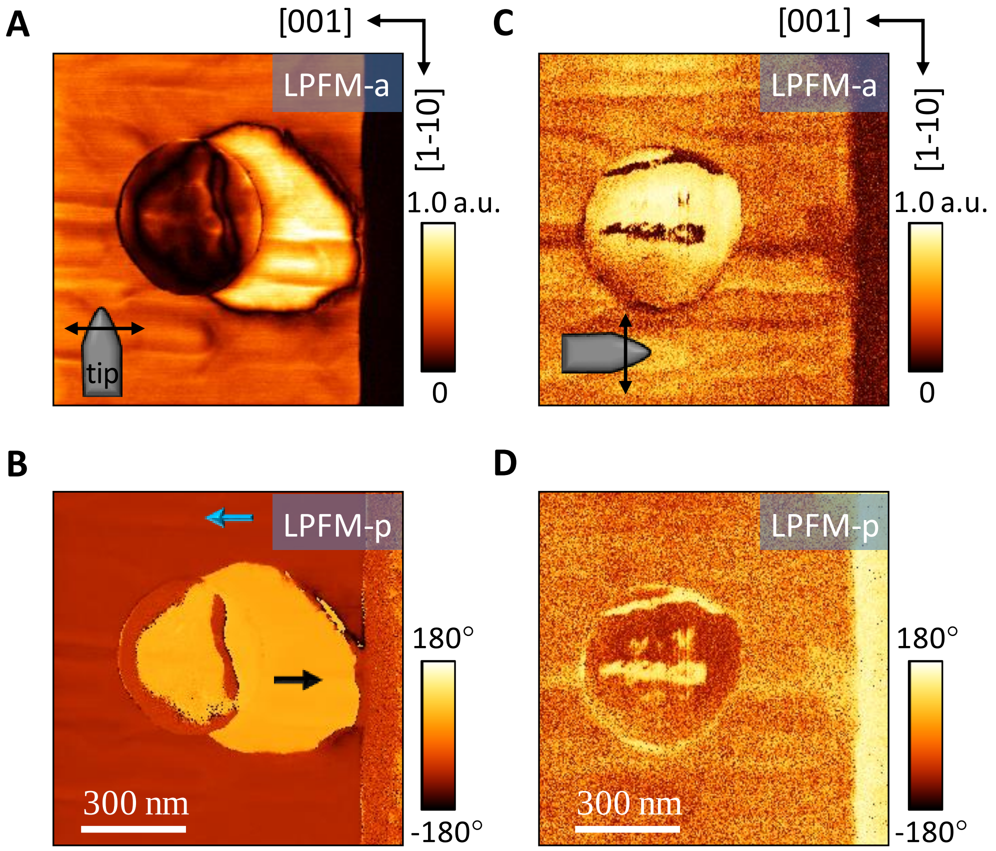

fig. S5. Vector PFM of the switched domain. (**A** to **B**) Lateral PFM amplitude (LPFM-a) (A), and the corresponding phase (LPFM-p) image (B) showing switched domain and domain walls with long axis of the cantilever along [-110] direction. (**C** to **D**) Lateral PFM amplitude (C), and the corresponding phase image (D) of the same area as in (A-B) after physical rotation of the sample by 90°, such that the long axis of the cantilever is along the [00-1] direction.

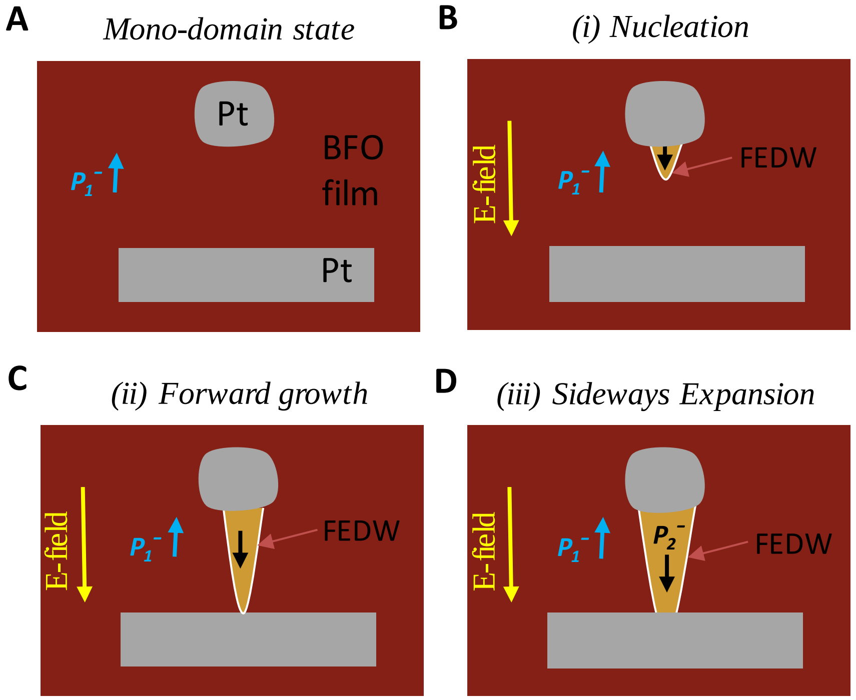

fig. S6. A schematic of the ferroelectric switching process (top view). (**A**) Initial mono-domain configuration. *Upon application of the external field between the metal electrodes:* (**B**) Creation of reversed polarized domain nucleus along with the simultaneous appearance of ferroelectric domain walls. (**C**) Rapid forward growth of the reversed polarized nucleus towards the opposing electrode. (**D**) Slower sideways expansion of the switched domain.

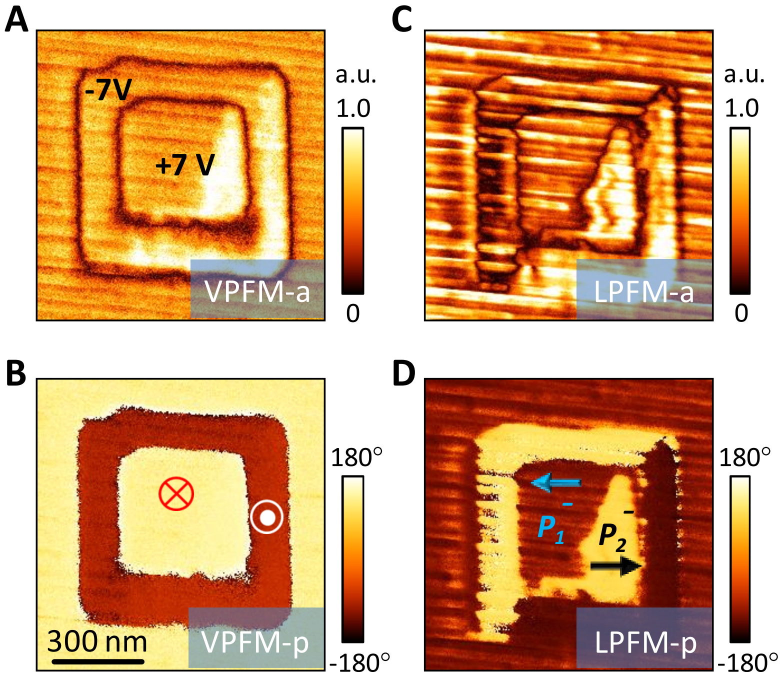

fig. S7. Electrical poling of the BFO/LSMO/STO (110). (**A** to **B**) Vertical PFM amplitude image (A), and the corresponding PFM phase image (B) respectively. (**C** to **D**) Lateral PFM amplitude image (C), and the corresponding PFM phase image (D) respectively for the same area as shown in images (A-B). These images were acquired after electrical poling of the concentric square regions (inner region: +7V, outer region: -7V) using a conductive SPM tip.

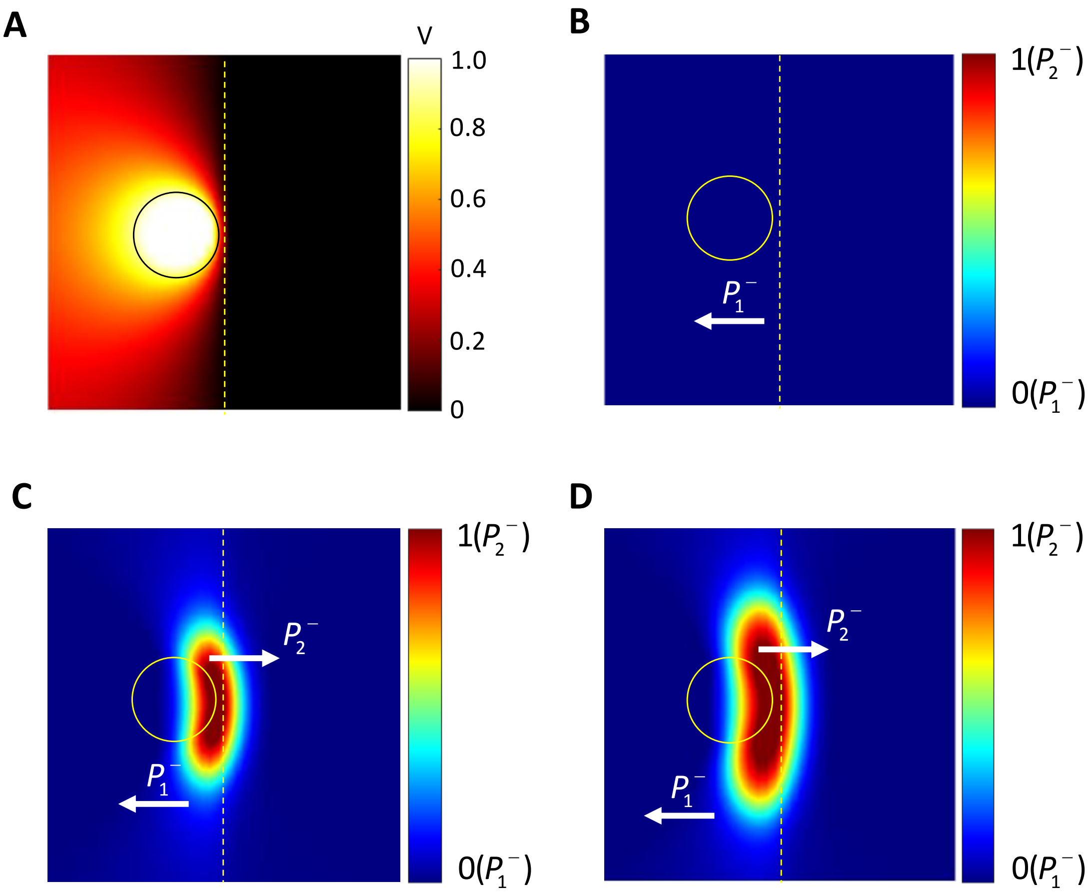

fig. S8. Numerical simulation of the switched ferroelastic domain. (**A**) Profile of electric potential (in normalized scale) induced by the platinum metal electrodes. (**B**) Initial configuration of the domain consisting of polarization variant P_1^-. (**C** to **D**) Phase field simulation of the switched domain in the intermediate state (C), and in equilibrium (D). In these images, circle represents the location of the small metal electrode, while the dashed vertical line represents the boundary of the large platinum plate. The color map/scale in images (B-D) shows the values of the characteristic function $\mu(\mathbf{x})$ representing occupation of the two variants of the polarization ($\mu(\mathbf{x})=1$ corresponds to P_2^-, while $\mu(\mathbf{x})=0$ corresponds to P_1^-). The characteristic function describes the topology, and has no physical unit.

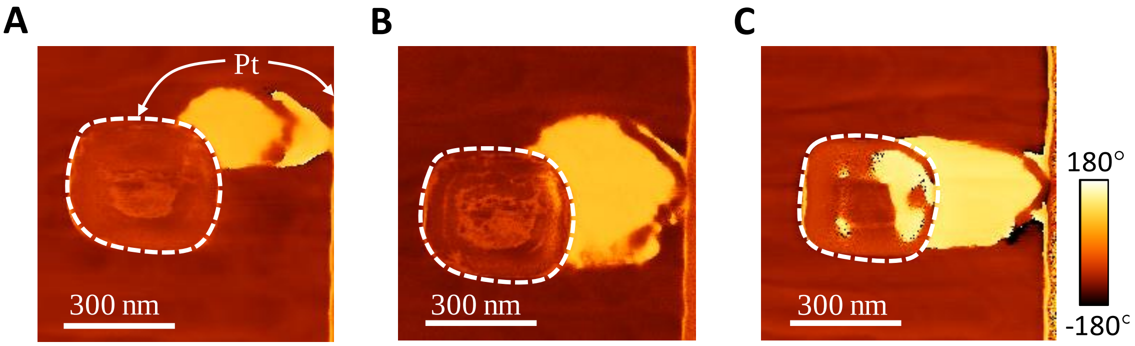

fig. S9. Triangular or the arrow-like shape of the switched domain. (**A** to **C**) LPFM phases images showing triangular or arrow-head like shape for switched domains of different sizes.

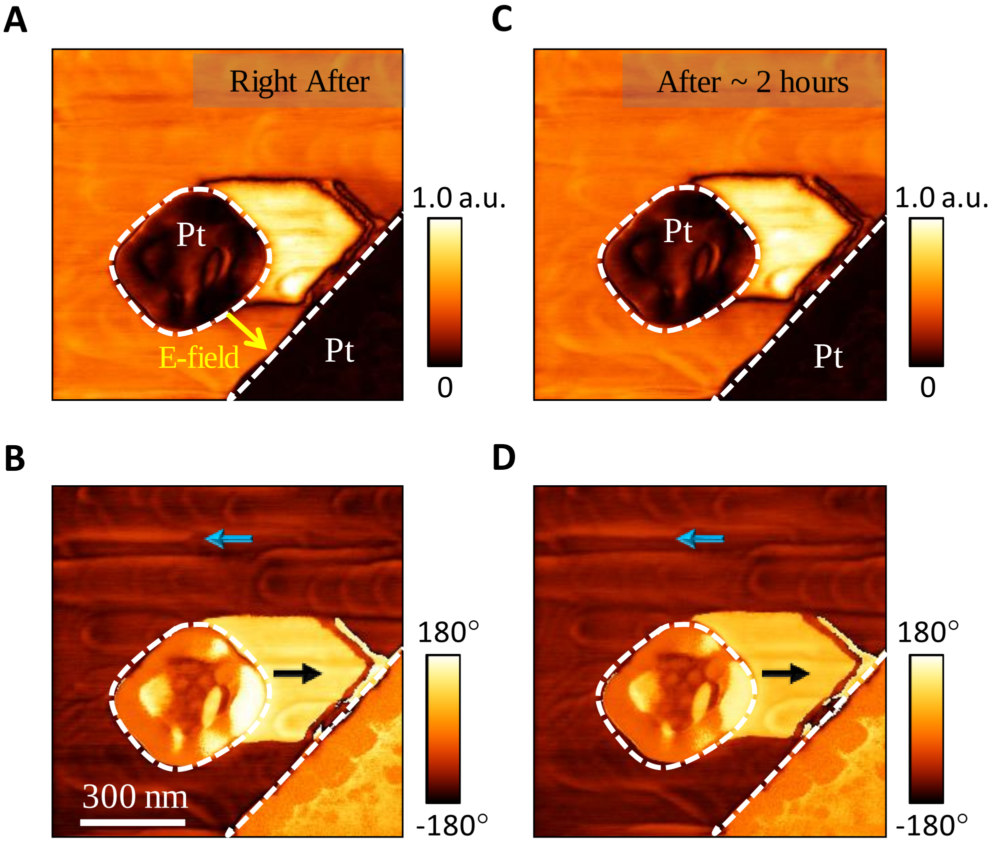

fig. S10. Switching via electric field oriented 45° to the in-plane polarization direction. (**A** to **D**) LPFM amplitude and the corresponding LPFM phase image acquired right after (A-B), and approx. two hours later (C-D) on creation of the switched domain respectively. Images in (A,C) are the LPFM amplitude images, while in (B,D) are the corresponding LPFM phase images.

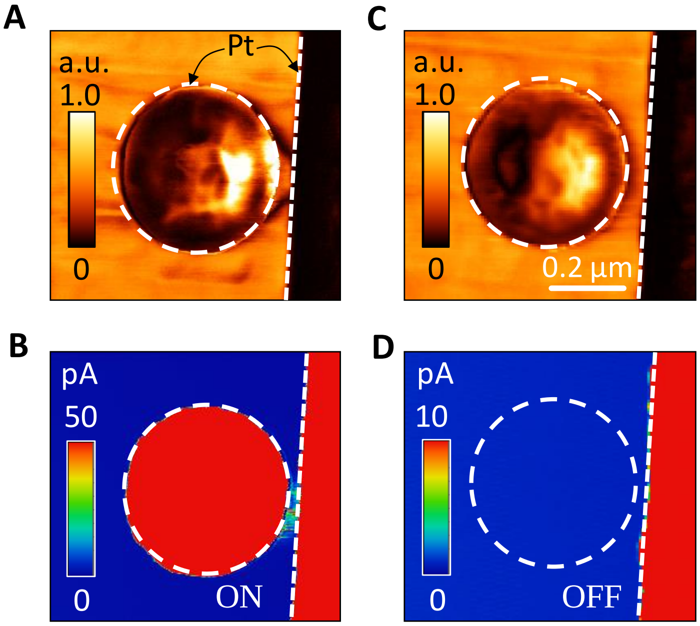

fig. S11. Sub–100-nm FEDW memory device. (**A** to **B**) Lateral PFM phase image (A), and the corresponding c-AFM map (B) respectively acquired in the presence of domain walls. (**C** to **D**) Lateral PFM phase image (C), and the corresponding c-AFM map (D) respectively acquired for the domain wall free state. The c-AFM maps were acquired non-invasively at a fixed DC read bias of +2.0V.

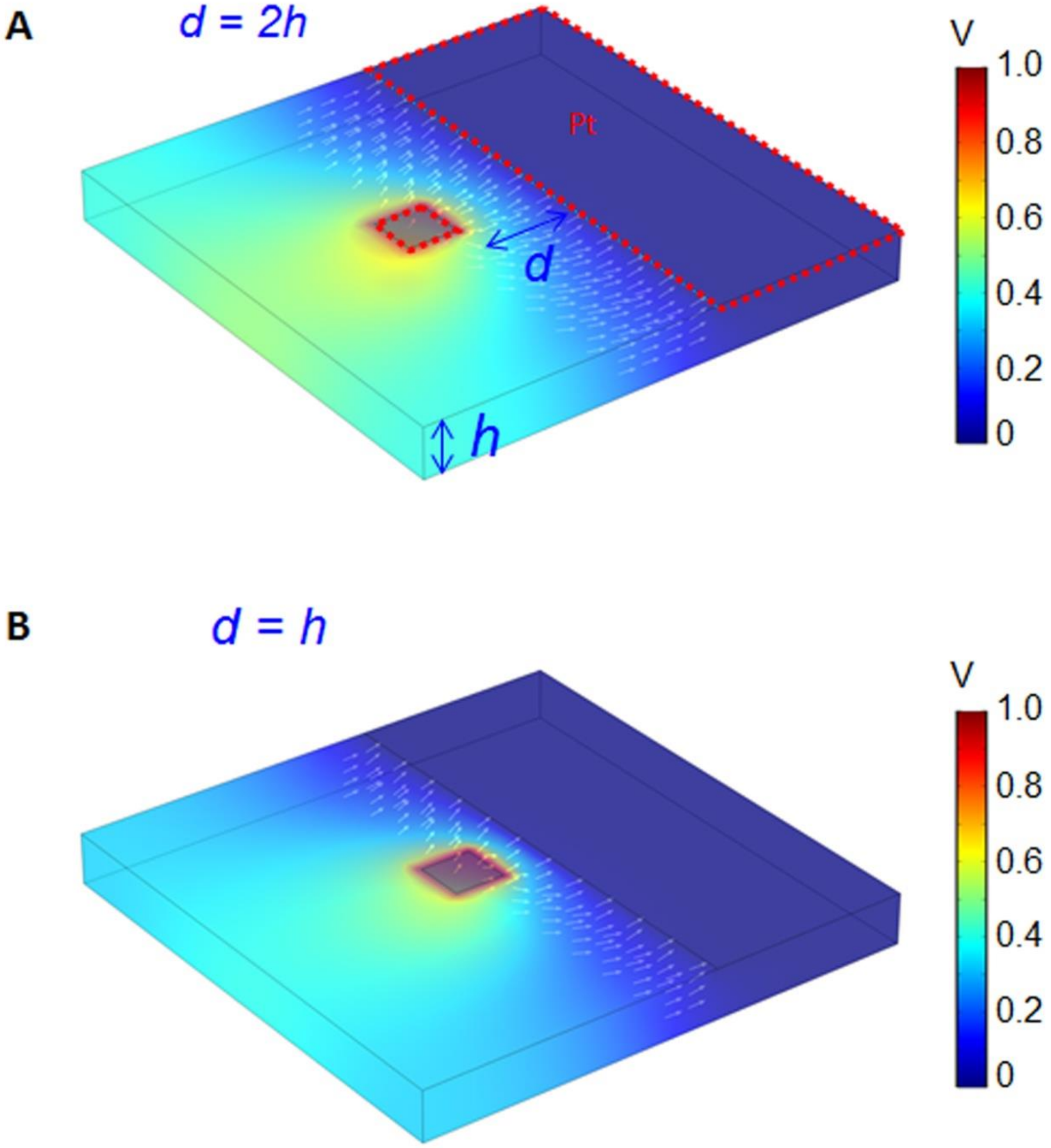

fig. S12. Potential and electric field distribution. The potential and electric field distribution generated by the platinum electrode pair for different ratios of the spacing (*d*) between the electrodes and thickness (*h*) of the $BiFeO_3$. (**A**) For d = 2h; (**B**) d = h. The color contour shows the electrical potential, while the arrows in white represent vectors of the electric fields. The Pt electrodes are shown by the small and large enclosed red dotted-rectangle in (A).

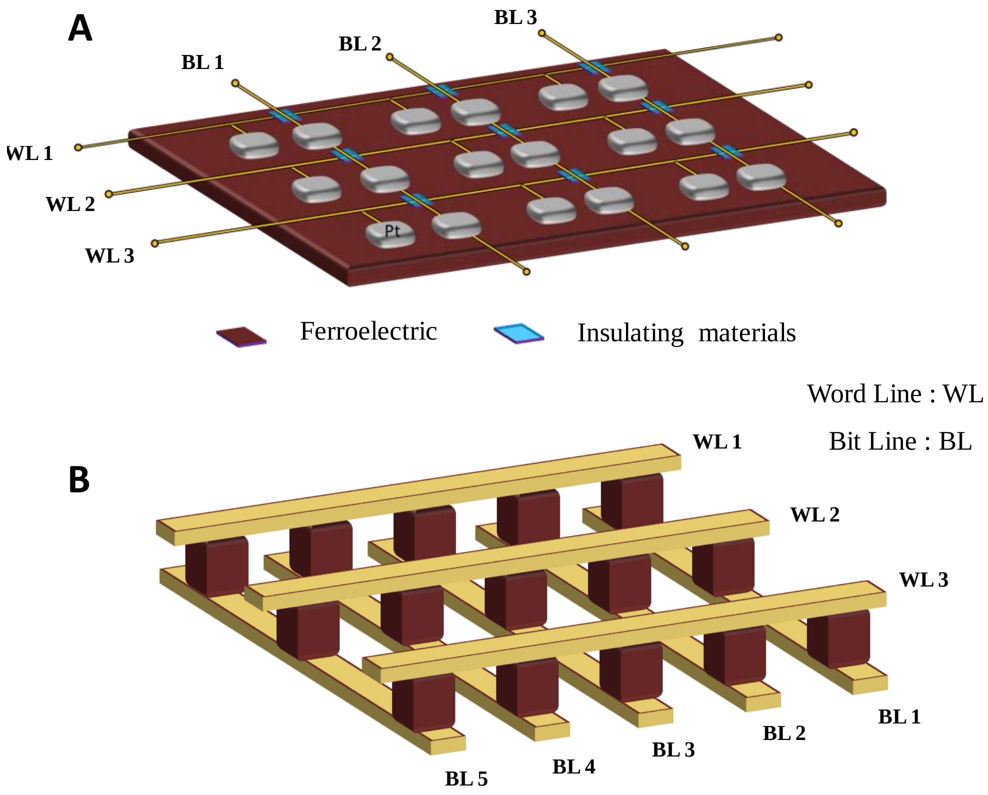

fig. S13. Integration of FEDW memory cell in an array structure. (**A**) A schematic of the (3 X 3) FEDW memory cells in an in-plane array structure. (**B**) A schematic of the (3 X 5) FEDW memory cells in a cross-bar array structure.